Direct Residual Stress Identification during Machining

Théo Jovani, Hélène Chanal, Benoît Blaysat, Michel Grédiac

Direct Residual Stress Identification during Machining

Théo Jovani*[a], Hélène Chanal[a], Benoît Blaysat[a], and Michel Grédiac[a]

[a]Université Clermont Auvergne, CNRS, Clermont Auvergne INP, Institut Pascal, F-63000 Clermont-Ferrand, France

Abstract Raw parts with high mechanical performances used for aeronautical workpieces are generally obtained by mechanical processes such as molding and/or forging. They mostly undergo additional heat treatments. These processes may induce mechanical residual stress within the material. During the machining step, residual stress are released when material is removed, which leads to initial stress distribution disruption. Thus, the workpiece deforms to satisfy the internal equilibrium, therefore requiring additional operations to be performed to fulfill dimensional and geometrical restrictions. A method has been developed here in order to identify residual stress maps within metal workpieces during machining. This method relies on the residual stress measuring method called "Layer Removal Method" and on a non-contact full-field measuring technique called "Digital Image Correlation". This development aims at improving traditional residual stress measuring techniques and to realize measurements under harsh conditions, namely during machining. Compared to classical measuring methods, the proposed one involves several improvements such as being a non-contact and optical measurement and being performed continuously during the machining process. This novel approach

*Corresponding author : theo.jovani@sigma-clermont.fr

allows the determination of the initial residual stress distribution across the depth by measuring the through-thickness workpiece displacement fields induced by the residual stress release during machining. A residual stress map within a Al7010-T7451 aluminum alloy beam with a magnitude order lying between -34 MPa and 36 MPa has been retrieved. Obtained results have been compared with literature- and Finite Elements results. This novel approach would ensure measurement of residual stress distributions of a part being machined, allowing monitoring and predicting, in real-time, part deflection. Therefore, adapting machining sequences in real-time would be possible to prevent undesirable deformations.

Keywords Residual Stress Distribution Retrieval ; Aeronautical Workpieces ; Layer Removal Method ; Global Digital Image Correlation ; During Machining Measurements.

Introduction

Aluminum parts used in aeronautics field must ensure high mechanical performance. To this end, raw materials of these workpieces are generally obtained by mechanical processes such as molding, rolling and/or forging. Additionally, in order to enhance their mechanical properties, raw materials undergo heat treatments, for example quenching, annealing and/or hardening. These operations may induce multi-axial residual stresses within the material [1], which remain within the material in the absence of any external forces applied to the part and under uniform temperature conditions [2]. These fields are composed of both compressive and tensile stresses, which combine to form a self-balanced distribution. Depending on the mechanical operations

and heat treatments the raw part has undergone, the residual stress distribution takes different shapes and magnitudes. This then influences the further shaping of the final machined part. Indeed, when a raw part is machined, mechanical residual stresses are released and the stress distribution is reorganized. A consequence is that the machined workpiece deforms in order to restore the internal equilibrium.

This deformation is notably high in the aeronautics field due to the slender design of the workpieces and because up to 90% of material is removed during the shaping step. This undesirable deformation represents a major issue for aircraft part manufacturers. Indeed, it induces costly and delicate additional operations. A study conducted by Boeing on four aircraft programs shows that the costs linked to workpiece distortion problems amount to 290 millions US dollars [3]. In the same study, it is stated that the probability of distortion causing deformation in thin-walled components, which are beyond the allowed tolerances, is about 47%. Furthermore, another study shows that the cost of re-work and scrap of deformed workpieces is excessively expensive for part manufacturers [4]. In this context, it is relevant to examine whether the effect of residual stresses could be accounted for *during* manufacturing. The underlying idea is to measure the deformation of the part between consecutive passes, and to adjust in real-time the parameters of the initial machining sequence to counterbalance the negative effect of residual stresses. This is one of the objective of the ANR IMaDe project, which aims at developing a smart machining cell to control the deformation of aeronautical workpieces during machining.

In this paper we address one of the tasks of this project, which consists of measuring during manufacturing the effect of residual stress release on the geometry of a specimen by using a

dedicated Digital Image Correlation (DIC) approach, and to deduce from this measurement the through-thickness residual stress distribution. Contrary to the techniques which are commonly used to retrieve residual stress maps such as Neutron diffraction or crack-compliance method [2, 5], the method proposed herein ensures retrieval of through-thickness residual stress distribution within thick components. It is based on an iterative surface milling similar to the so-called Layer Removal Method (LRM). The latter method was first introduced by Treuting in 1951 in order to retrieve rolling and transverse residual stress distributions in sheet materials [6]. It involves the removal of thin layers by milling the raw part to be characterized. At the end of each layer removal, the workpiece is unmounted from the machine table in order to measure the induced curvatures. Then, the through-thickness residual stress distribution is derived from these measurements. The major issue with this technique is that the workpiece has to be unclamped from the machine tool each time curvature needs to be measured. The aim of this paper is to introduce a method which enable us to measure the through-thickness residual stress map without unclamping. However, previous studies have shown that the clamping system has a significant impact on the workpiece deformation when residual stresses are released [7]. Indeed, if the clamping system is too restrictive, the part will not be able to deform sufficiently to restore the residual stress equilibrium, leading thus to remaining compressive and/or tensile forces within the material. In the suggested method, precautions are taken regarding the positioning as well as the clamping system in order to minimize their impact on the residual stress equilibrium during machining, and therefore on the final workpiece deformation.

The idea here was to rely on DIC to perform part deflection measurements directly in the machine tool workspace during the shaping process. Previous study shows the potential ben-

efit of using DIC for workpiece deformation measurements during machining [8]. Contrary to common measurement devices such as strain gages or lasers, which provide point-wise measurements [9], DIC provides full-field measurements. Moreover, DIC has also proven its effectiveness in the manufacturing field [10] as well as in retrieving residual stress distributions [11, 12].

The novel method presented in this article is based on the LRM machining strategy coupled with a Global Digital Image Correlation (GDIC) method. GDIC ensures to integrate predicted deformation models in order to determine the deformations induced by the residual stress release, and to retrieve the initial through-thickness stress distribution. Moreover, non-contact measurements are obtained with GDIC, thus allowing the workpiece to remain clamped during machining.

This paper is organized as follows. Firstly, the model of the residual stress release inducing workpiece deformations as well as its measurement is introduced. The GDIC method presently deployed as well as the deformation models used to predict the workpiece deflection are then outlined. Finally, the experimental setup is described, and the results are illustrated and discussed.

1 Residual stress release during the machining of a beam

In this paper, the LRM machining strategy is adopted in order to retrieve the initial through-thickness residual stress distribution within a beam during its machining. The procedure consists of removing layers at the top of the beam to be characterized. The classic version of LRM involves the workpiece to be successively unclamped from the machine table in order to

measure the curvature induced by the residual stress release. A relationship between successive beam curvature and the initial residual stress distribution has been established in [13]. In this reference, the layers are chemically removed from the bottom of the part. This approach has been adapted here to a machining from the top of the part. The proposed model is illustrated in Fig.(1).

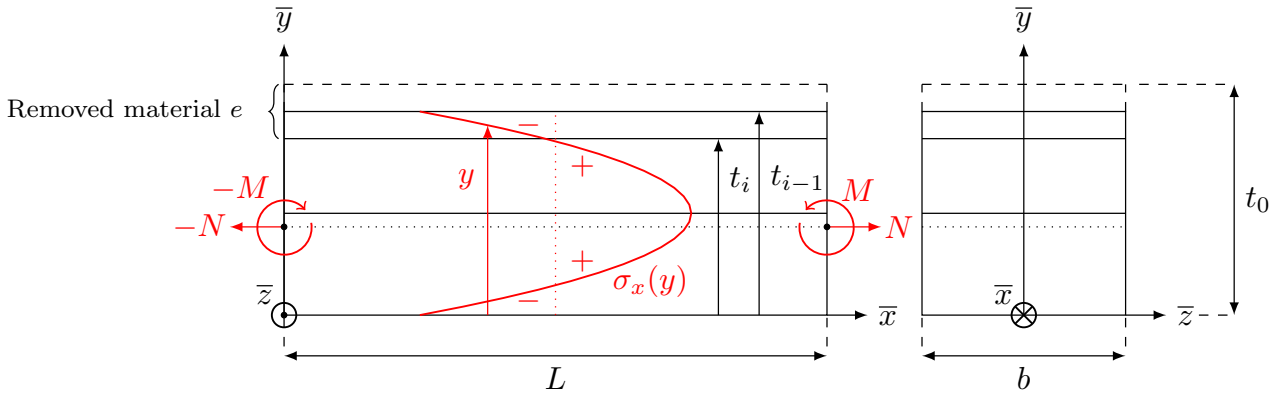

Figure 1: Layer Removal Method model from [13] adapted here to a machining from the top of the beam. The figure is presently depicting the machining of the i^{th} layer and the residual stress distribution denoted by σ_x is represented here in an arbitrary way.

In this paper, only the residual stress distribution along the rolling direction of the beam ($\overline{x}$-axis) is studied. The residual stress distribution is assumed to only depend on the thickness [13]. Nevertheless, it is significant to point out that independently of the cutting conditions, residual stresses are generated by the machining process within the top layer of the workpiece. However, it has been demonstrated that the depth impacted by the residual stresses caused by machining is always less than 250 μm when milling aluminum alloys [14]. Thus, their effect on the macroscopic response of the workpiece with a thickness of several millimeter order is

negligible. The sought residual stress distribution is denoted by σ_x. The material is considered to be isotropic and elastic constant are assumed to be the same throughout the specimen. As the distribution is continuous and the machining discrete, the stress map identification is performed under two assumptions : (1) the residual stress distribution is reorganized in order to satisfy the internal equilibrium of the beam, (2) the released stresses are considered as an external load which induces a bending moment M and a normal force N at the neutral plane of the remaining part of the beam (see Fig.(1)). The normal force N may be neglected [13] and deformations are assumed to remain in the elastic domain. The bending moment M therefore induces the deflection of the beam. At a given beam abscissa x, the moment induced by the residual stress release with respect to the neutral plane of the remaining part of the beam is expressed as follows [2] :

$$M = b \int_{t_i}^{t_0} \left(y - \frac{1}{2}(t_0 - e) \right) \sigma_x(y) \mathrm{d}y \tag{1}$$

where b is the beam width, t_0 is the initial beam thickness, t_i $(= t_0 - e)$ the thickness of the beam after the removal of the i^{th} layer, e is the thickness of the removed material and σ_x is the residual stress distribution throughout the beam thickness. These notations are illustrated in Fig.(1).

Considering that deformations remain in the elastic region, classical beam theory is applicable. The bending moment along the beam is also expressed as follows [15] :

$$M(x) = EI\gamma(x) = E \frac{b\, t^3}{12(1-\nu^2)} \gamma(x) \tag{2}$$

where E is the Young's modulus, I is the quadratic moment of area of the cross-section, ν is

the Poisson's ratio and γ is the beam curvature.

The thickness of the beam and its curvature evolve throughout the machining process at the end of each milling operation, thus by increasing the thickness of the removed material e. Therefore, the variation of the induced moment M is determined by differentiating Eq.(1) with respect to the thickness of the removed material. The following expression from [13] is obtained from Eq.(1) by using the LEIBNIZ rule [16] :

$$\frac{dM}{de} = b\left[\frac{t_i}{2}\sigma_x(t_i) + \frac{1}{2}\int_{t_i}^{t_0}\sigma_x(y)\mathrm{d}y\right] \tag{3}$$

$\frac{dM}{de}$ can also be obtained by differentiating Eq.(2) with respect to e :

$$\frac{dM}{de} = \frac{bE}{12(1-\nu^2)}\left[t_i^3\frac{d\gamma}{de} + \gamma\frac{dt_i^3}{de}\right] \tag{4}$$

The expression of the initial residual stress distribution can be deduced from Eq.(3) and (4) :

$$\sigma_x(t_i) = \frac{\frac{E}{12(1-\nu^2)}\left[t_i^3\frac{d\gamma}{de} + \gamma\frac{dt_i^3}{de}\right] - \frac{1}{2}\int_{t_i}^{t_0}\sigma_x(y)\mathrm{d}y}{\frac{t_i}{2}} \tag{5}$$

As the machining strategy incrementally removes layers, the removal of the material is performed piecewise, which leads Eq.(5) to be rewritten in an incremental form. Considering the machining of the i^{th} layer, the thickness reduces from t_{i-1} to t_i and the curvature becomes γ_i instead of γ_{i-1}. Besides, assuming average values for thicknesses and curvatures and that residual stresses are constant within a removed layer, Eq.(5) can be rewritten in order to express

the average residual stress value after the removal of the i^{th} layer [13] :

$$\sigma_{x_i} = \frac{\frac{E}{12(1-\nu^2)}\left(t_i^3\gamma_i - t_{i-1}^3\gamma_{i-1}\right) - \frac{1}{2}\Delta e_i \sum_{n=1}^{i-1}\left(\sigma_{x_n}\Delta e_n\right)}{\frac{1}{2}\Delta e_i\left(\frac{t_i + t_{i-1}}{2}\right)} \tag{6}$$

where $\Delta e_i = t_{i-1} - t_i$ and t_i and γ_i respectively denote the thickness and the curvature of the beam at the end of the machining of the i^{th} layer.

Eq.(6) iteratively gives the value of the residual stress distribution within the beam after the removal of each layer i. This distribution only depends on the successive beam thicknesses and curvatures, and also on the material properties. This expression enables us to determine the residual stress distribution σ_x by calculating incrementally its values by only measuring the beam curvature after each layer removal. With the procedure proposed in [13], the beam has to be unmounted from the machine table in order to measure its curvature with metrological tools. The curvature is measured with this approach at the middle of the part to avoid edge effects.

The method proposed in this paper is intended to let the workpiece remaining clamped on the machine tool. The middle curvature of the clamped workpiece is assumed to be identical to the curvature of the workpiece when it is unclamped. The benefit of this hypothesis is to identify the same initial residual stress map retrieved by the traditional LRM, but while allowing the workpiece to remain mounted on the machine tool. To reach this goal, precautions have been taken concerning the workpiece positioning and clamping systems. In our experiment,

the workpiece was raised at its ends by two wedges and clamped onto the workpiece holder solely by two flanges placed at its ends. The interested reader may refer to Section (4) for more details about the mounting setup. With this procedure, it was expected to minimize the impact of both positioning and the clamping systems on the deflection of the workpiece, and to give to the workpiece more freedom to deflect at its center.

DIC has been used to measure successive curvatures while letting the workpiece clamped during milling. The DIC problem formulation is detailed in the next section.

2 Tuning Digital Image Correlation for robustly identifying the Residual Stress distribution during Machining

Digital Image Correlation (DIC) was introduced in the 1980s [17]. Since then, it has become widely diffused in the experimental mechanics community. DIC relies on images of a specimen under loading in order to retrieve its displacement field. The ease of its implementation, requiring only a camera, has greatly facilitated its dissemination. DIC is based on the numerical processing of two pictures taken at two different load levels of a mechanical component undergoing deformations. Contrary to usual measurement techniques such as strain gages, position sensors or measuring probes [9], DIC offers full-field measurements and retrieves displacements at any point of the observed surface. The contrast of the surface of interest is generally en-

hanced by painting a speckle onto it. The features of this speckle pattern are followed by the DIC algorithm. The monitored region is referred as the Zone of Interest (ZoI). It is composed of pixels containing gray level values. Considering a picture f of the workpiece reference state, each pixel $P : \overline{x_P} = x\overline{x} + y\overline{y}$ inside the ZoI has a gray level value denoted by $f(\overline{x_P})$. When the workpiece deforms and assuming the speckle texture is preserved, the latter is supposed to be subjected to the same displacement field $\overline{u}$ of the surface. Considering another picture g of the specimen, each pixel P that compose it has undergone the displacement field $\overline{u}$. The gray level values at this pixel is denoted by $g(\overline{x_P} + \overline{u}(\overline{x_P}))$. A typical example of a speckle undergoing a displacement field $\overline{u}$ between two beam states is given Fig.(2).

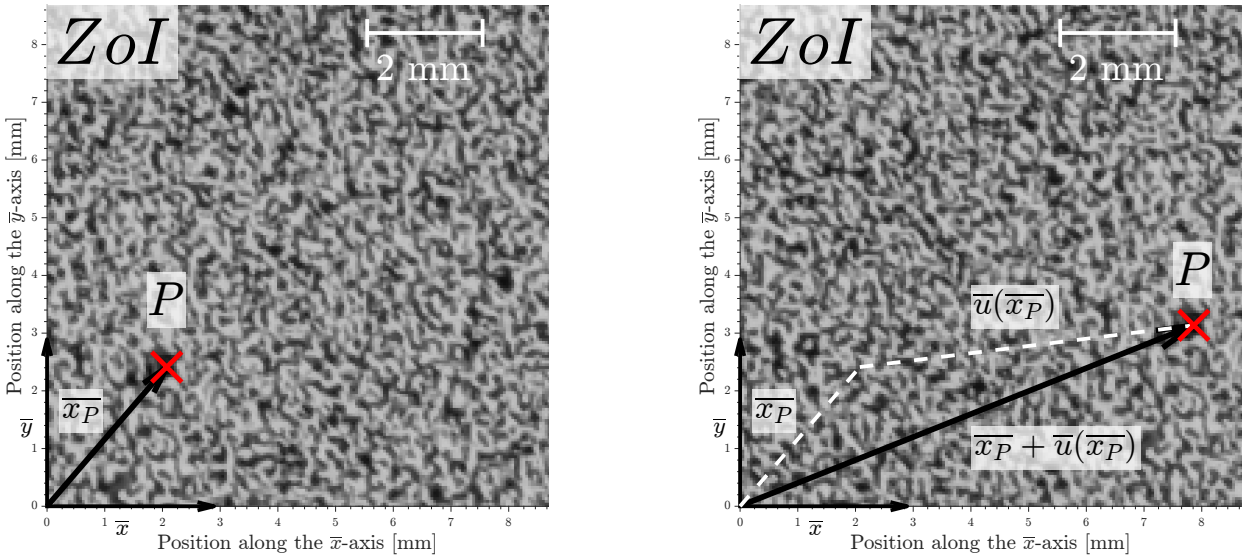

(a) Reference state, picture f.

(b) Deformed state, picture g.

Figure 2: Close up of the considered speckle texture.

DIC is based on the conservation of the optical flow between two pictures [18]. It means that the brightness is conserved for all the N_P pixels of the ZoI. This conservation writes as

follows [18]:

$$\forall\, \overline{x_P} \in \{1, \dots N_P\}, \qquad f(\overline{x_P}) - g(\overline{x_P} + \overline{u}(\overline{x_P})) \approx 0 \tag{7}$$

The goal of DIC is to retrieve the displacement field $\overline{u}$ from Eq.(7). However, retrieving displacement field $\overline{u}$ from Eq.(7) is an ill-posed problem. Indeed, it consists of determining both components of the displacement field $\overline{u}$ based only on the gray level value of a pixel, which is a scalar quantity. A usual regularization of this problem consists of taking a subset of the ZoI, referred as Region of Interest (RoI), and introducing a set of shape functions $\mathcal{U}$, which approximates the displacement field of the RoI, denoted by $\overline{u_{RoI}}$. The set of shape functions $\mathcal{U}$ is composed of m functions $(\overline{\varphi_i})_{1\leq i\leq m}$. Hence, the displacement field is fully described over the RoI with m Degrees of Freedom (DoFs) listed by $(\lambda_i)_{1\leq i\leq m}$ and is expressed as follows :

$$\forall\, \overline{x_P} \in RoI, \qquad \overline{u_{RoI}}(\overline{x_P}, \boldsymbol{\lambda}) = \sum_{i=1}^{m} \lambda_i \overline{\varphi_i}(\overline{x_P}) \tag{8}$$

In addition, a concern while performing DIC is that the optical flow between two pictures is not totally preserved. To mention only two, the noise of the camera sensor and a heterogeneous lighting of the speckle texture are sources of this non-conservation. Moreover, in the context of machining, the optical flow is highly disturbed because of the presence of metal chips. Thus, Eq.(7) is relaxed to a residual whose norm is minimized over the RoI with respect to the sought displacement field. This reformulation is based on the Sum of Squared Difference (SSD) criterion [19] and defines the optimized DoFs :

$$\boldsymbol{\lambda}_{\mathbf{opti}} = \underset{\boldsymbol{\lambda}^* \in \Re^m}{\operatorname{argmin}} \left[\sum_{\overline{x_P} \in RoI} \left(f(\overline{x_P}) - g\left(\overline{x_P} + \sum_{i=1}^{m} \lambda_i^* \overline{\varphi_i}(\overline{x_P}) \right) \right)^2 \right] \tag{9}$$

where $\boldsymbol{\lambda}_{\mathbf{opti}}$ is a $m \times 1$ vector, which contains the optimized DoFs values describing the dis-

placement field $\overline{u_{RoI}}$ and minimizing the residual norm between the two pictures.

In order to solve Eq.(9), a modified GAUSS-NEWTON scheme is used [20]. It provides the optimized DoFs $\boldsymbol{\lambda}_{\mathbf{opti}}$ by incrementally updating $\boldsymbol{\lambda}$ from an initial guess $\boldsymbol{\lambda}^{\mathbf{0}}$ with the following scheme :

$$\boldsymbol{\lambda}^{k+1} = \boldsymbol{\lambda}^{k} + \delta\boldsymbol{\lambda}^{k} \qquad \text{with} \qquad \delta\boldsymbol{\lambda}^{k} = \mathbf{M}^{-1} \times \mathbf{L} \times \boldsymbol{\Psi}(\boldsymbol{\lambda}^{k}) \tag{10}$$

where,

- vector $\boldsymbol{\Psi}(\boldsymbol{\lambda}^{k})$ corresponds to the optical residual at any pixel such as :

$$\forall i \in \{1, \ldots, m\}, \forall j \in RoI, \qquad [\boldsymbol{\Psi}(\boldsymbol{\lambda}^{k})]_j = f(\overline{x_j}) - g\left(\overline{x_j} + \sum_{i=1}^{m} \lambda_i^k \overline{\varphi_i}(\overline{x_j})\right); \tag{11}$$

- matrix $\mathbf{L}$ corresponds to the subset shape functions projected onto the reference image gradient such as :

$$\forall i \in \{1, \ldots, m\}, \forall j \in RoI, \qquad [\mathbf{L}]_{ij} = \overline{\nabla f}(\overline{x_j}) \cdot \overline{\varphi_i}(\overline{x_j}); \tag{12}$$

- and matrix $\mathbf{M}$ corresponds to the DIC tangent operator, more commonly called "correlation matrix". It is defined by :

$$\mathbf{M} = \mathbf{L} \times \mathbf{L}^{-1}. \tag{13}$$

The interested reader may refer to [21] for detailed calculations of $\mathbf{L}$ and $\mathbf{M}$. The convergence criterion of the DIC algorithm is often defined by the value of the Euclidean norm of $\delta\boldsymbol{\lambda}^{k}$ compared to a threshold value C_{Crit}, chosen here to be equal to $C_{Crit} = 10^{-6}$ [21]. The set of shape functions $\mathcal{U}$ is then defined in order to iteratively compute the updated quantity $\delta\boldsymbol{\lambda}^{k}$. It is detailed in the next section.

3 Subset Shape functions

The *RoI* displacement field $\overline{u_{RoI}}$ is defined by a set of shape functions weighted by their respective DoFs, see Eq.(8). This set depends on the DIC method which is adopted. In the literature, two main approaches exist : the local and the global versions. A detailed comparison between them and their respective use may be found in [22]. In the case of Local DIC, small $RoIs$ and a simple set of shape functions $\mathcal{U}$ are used. The shape functions mostly rely on low order polynomials such as rigid-body motion functions. For Global DIC (GDIC), a large *RoI* and a more elaborated set are chosen. To mention only a few, typical used shape functions are Chebyshev polynomials, Finite Element functions or NURBS [23]. In this paper, the chosen *RoI* matches the ZoI, which corresponds to the entire beam surface monitored with the camera. The objective here is to fully describe the workpiece displacement field of the beam, especially at its ends. An advanced set $\mathcal{U}$ is also defined in order to describe the displacement field $\overline{u_{RoI}}$ thanks to the beam theory, in Section (3.2).

DIC implementation to measure the deflection of the part during machining was realized in [8]. Considering the camera is mounted on the machine table, it is subjected to machine tool vibrations. Rebergue *et al.* showed that it is relevant to use two *RoIs* to clearly distinguish the workpiece deformation induced by the milling process on the one hand, and rigid-body movements of the camera with respect to the workpiece on the other hand. In our case, speckles were deposited onto the monitored surface of the beam and also onto the surface of the workpiece holder, as illustrated in Fig.(3) :

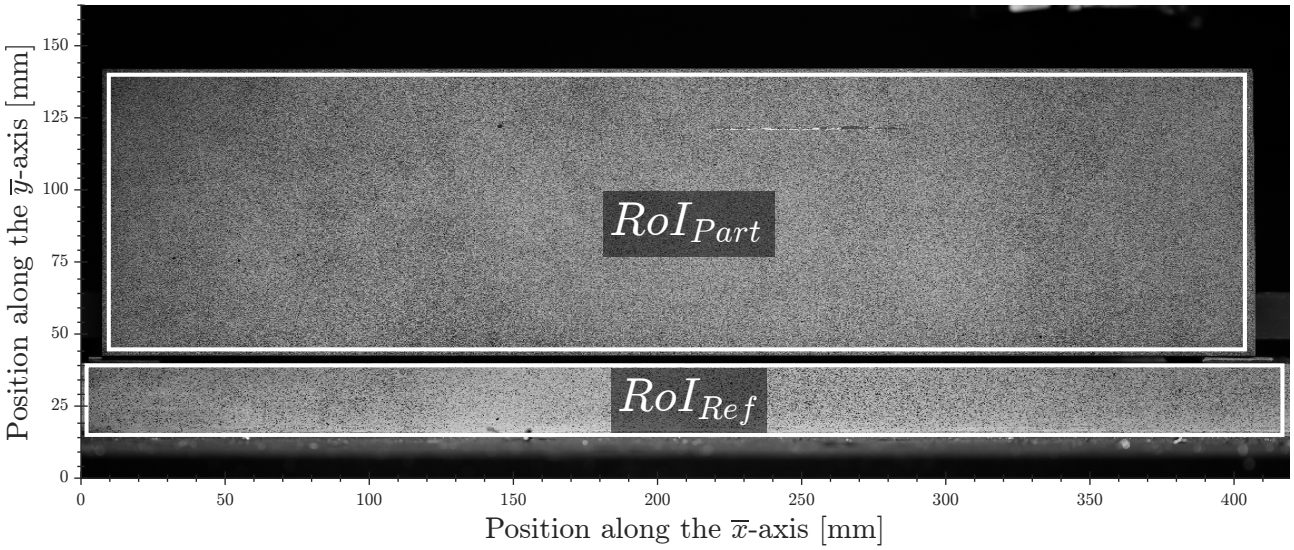

Figure 3: Speckles and *RoIs* definition. Since the workpiece holder is supposed not to deform, RoI_{Ref} is used to determine the camera rigid-body motion and RoI_{Part} is used to retrieve the global displacement field of the workpiece.

Two shape function sets were elaborated in order to describe respectively the rigid-body motions of the camera $\overline{u_{Ref}}$ and the global displacement field of the workpiece $\overline{u_{Part}}$. This latter displacement field includes both the camera rigid-body motion and the sought beam-like deflection due the to residual stress release. Hence, coupled with $\overline{u_{Ref}}$, it is used to extract the workpiece displacement field solely induced by the residual stress release, denoted by $\overline{u_{RS}}$. By defining each *RoI* displacement field as in Eq.(8), $\overline{u_{RS}}$ can be expressed as follows :

$$\begin{aligned} \overline{u_{RS}}(\overline{x_P}) &= \overline{u_{Part}}(\overline{x_P}, \boldsymbol{\lambda}_{\mathbf{Part}}) - \overline{u_{Ref}}(\overline{x_P}, \boldsymbol{\lambda}_{\mathbf{Ref}}) \\ &= \sum_{i=1}^{m_{Part}} \lambda_{Part_i} \overline{\varphi_{Part_i}}(\overline{x_P}) - \sum_{i=1}^{m_{Ref}} \lambda_{Ref_i} \overline{\varphi_{Ref_i}}(\overline{x_P}) \end{aligned} \tag{14}$$

The different shape function sets denoted by $\overline{\varphi_{Ref}}$ and $\overline{\varphi_{Part}}$ are detailed in the next sections.

3.1 Rigid-body motions

During machining, the camera undergoes a rigid-body motion which can be identified due to the texture of the workpiece support. A versatile description of $\overline{u_{Ref}}$ is implemented here. The four corners of the images define the nodes of a quad4-isogeometric element. The corresponding kinematics are thus the linear interpolations of the nodal displacements, leading $\overline{u_{Ref}}$ to be defined as follows [24] :

$$\overline{\varphi_{Ref_i}}(\overline{x_P}) = \frac{1}{4}\left(1+\alpha_i\left(\frac{2x}{a}-1\right)\right)\left(1+\beta_i\left(\frac{2y}{b}-1\right)\right) \tag{15}$$

where $(\alpha_i, \beta_i) = \{(1,1),(1,-1),(-1,-1),(-1,1)\}$ and (a,b) are the picture dimensions respectively along the $\overline{x}$- and $\overline{y}$-axis.

Rigid-body motions and first-order strain are exactly described, which corresponds here to the effect of camera movements. Fig.(4) illustrates the displacement of the four corners of the picture thanks to a quad4-isogeometric element.

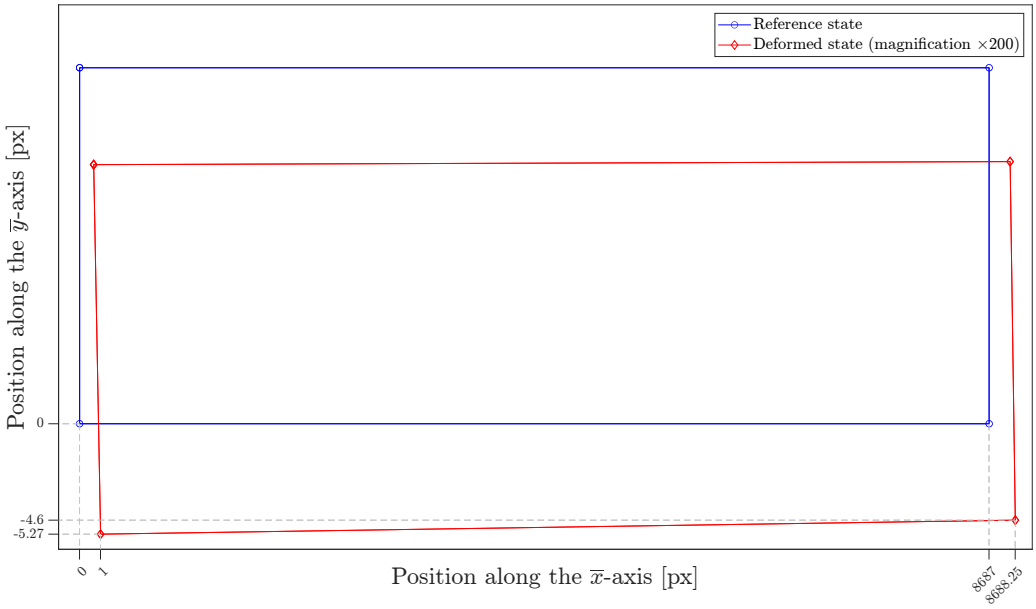

Figure 4: Illustration of the displacement of the four corners of the picture (here : after the machining of the 68^{th} layer).

The same functional space is also used for describing the gray level fluctuation that may occur during the experiments. Finally, Fig.(5) and (6) illustrate, respectively along the $\overline{x}$- and $\overline{y}$-axis, the rigid-body movement of the camera caused by vibrations.

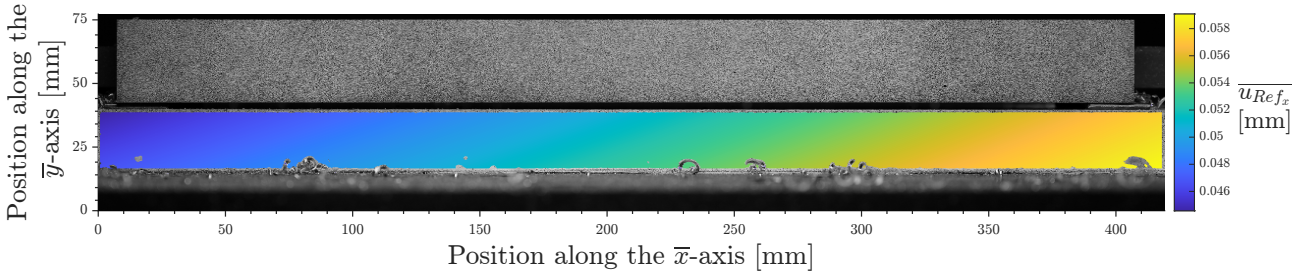

Figure 5: Typical camera rigid-body motion retrieved along the $\overline{x}$-axis. It is caused by the machine vibrations (here : after the machining of the 68^{th} layer).

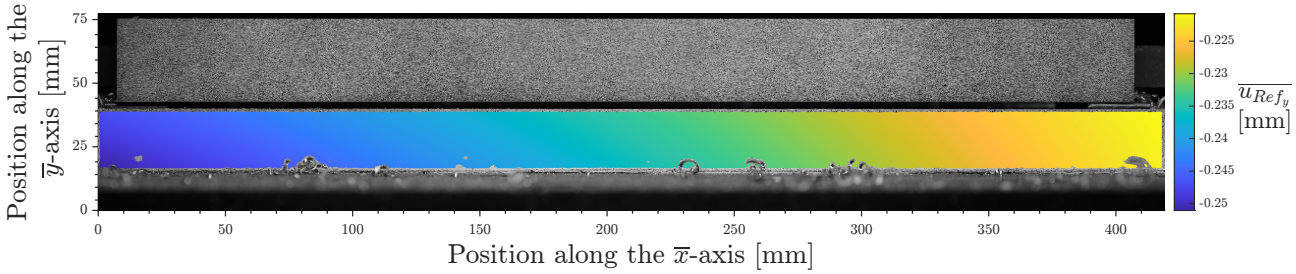

Figure 6: Typical camera rigid-body motion retrieved along the $\overline{y}$-axis. It is caused by the machine vibrations (here : after the machining of the 68^{th} layer).

3.2 Beam-like deflection

The workpiece displacement field $\overline{u_{Part}}$ is retrieved via a GDIC algorithm applied on RoI_{Part}. As explained in Section (3), the set of shape functions shall be able to describe a beam-like deflection since a GDIC method is adopted. A finite element method is employed to describe the workpiece geometry and to define the associated shape functions. The beam is supposed to satisfy the Euler-Bernoulli hypothesis which states that cross-section of the beam remains straight, inextensible and perpendicular to the neutral fiber of the beam after deformation. Considering this hypothesis, a Finite Element description, similar to [24], is implemented. The beam is horizontally discretized in N_k 2D-beam elements (here : $N_k = 10$) featuring two nodes with three DoFs each, as shown in Fig.(7).

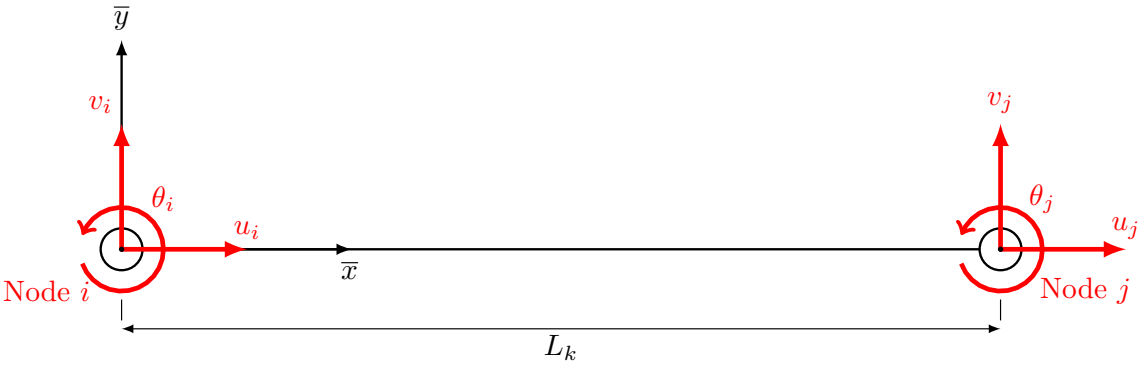

Figure 7: 2D-beam element with two nodes featuring three DoFs each.

Considering an element k, its displacement field $\overline{u_k}$ is expressed in the following matrix form $\overline{u_k}(\overline{x_P}, \boldsymbol{\lambda_k}) = \boldsymbol{\Phi_k}\boldsymbol{\lambda_k}$, where $\boldsymbol{\Phi_k}$ is the matrix of the shape functions of the element k, given in [25], and $\boldsymbol{\lambda_k}$ is the vector of the DoFs of the element k. Thus,

$$\overline{u_k}(\overline{x_P}, \boldsymbol{\lambda_k}) = \begin{bmatrix} 1-\xi & 0 \\ 6\eta(\xi-\xi^2) & 1-3\xi^2+2\xi^3 \\ L_k\eta(-1+4\xi-3\xi^2) & L_k\xi(1-2\xi+3\xi^2) \\ \xi & 0 \\ 6\eta(\xi^2-\xi) & \xi^2(3-2\xi) \\ L_k\eta(-3\xi^2+2\xi) & L_k\xi^2(\xi-1) \end{bmatrix}^T \begin{bmatrix} u_i \\ v_i \\ \theta_i \\ u_j \\ v_j \\ \theta_j \end{bmatrix} \tag{16}$$

where $\xi = \dfrac{x}{L_k}$ and $\eta = \dfrac{y}{L_k}$ are the normalized coordinates of a material point of the beam.

Consequently, the shape functions and the DoFs describing the displacement field of the beam $\overline{u_{Part}}$ are defined element-wise as follows :

$$\overline{\varphi_{Part}} = [\boldsymbol{\Phi_1}, ..., \boldsymbol{\Phi_{N_k}}] \qquad \text{and} \qquad \boldsymbol{\lambda_{Part}} = [\boldsymbol{\lambda_1}, ..., \boldsymbol{\lambda_{N_k}}] \tag{17}$$

The interested reader may refer to appendix (A) where the assumptions used to determine the shape function of the 2D-beam element are detailed.

As explained in Section (3), $\overline{u_{Part}}$ is also impacted by the rigid-body motion of the camera. Hence, the results separately obtained on RoI_{Ref} must be subtracted from their counterparts obtained on RoI_{Part} in order to isolate the displacement field solely due to the residual stress release, as expressed in Eq.(14).

4 Experimental setup and measurement methods

The procedure presented in this paper has been applied to an Al7010-T7451 aluminum-alloy beam of dimensions $400 \times 100 \times 100\,\mathrm{mm}^3$. 86 layers of thickness $e = 1$ mm have been successively machined from the top surface of the beam by using a 5-axe CRENO HSM (High-Speed Machining) machine tool of nominal power of 12 kW equipped with an electrospindle HSD ES799. The successive milling operations have been carried out with a Sandvik R590-110504H-NL H10 D100 milling cutter with six Sandvik R590-110504H-NL H10 inserts. The working tool was mounted on a HSK 63F tool holder. The cutting parameters are presented in Table 1. Fig.(8) shows the machined beam in its initial and final states. Between each milling operation, a waiting time of 10 minutes is set to ensure the workpiece to reach ambient temperature [8]. The underlying idea is that the workpiece has sufficient time to cool-down to ensure a stable equilibrium of the residual stress distribution before taking a picture and machining the next layer.

Table 1: Cutting parameters with Z number of teeth, V_c cutting speed, f_z feed rate per tooth, V_f feed rate, a_p depth of cut and N spindle speed.

Tool	Diameter (mm)	Z	V_c ($\mathrm{m.min^{-1}}$)	f_z ($\mathrm{mm.r^{-1}.teeth^{-1}}$)	V_f ($\mathrm{mm.min^{-1}}$)	a_p (mm)	N ($\mathrm{r.min^{-1}}$)
Milling cutter	100	6	1000	0.1	1911	1	3183

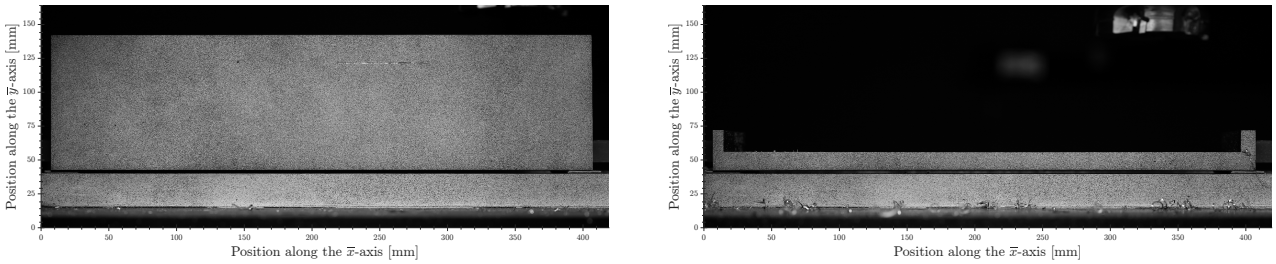

(a) Picture of raw geometry

(b) Picture of final geometry

Figure 8: Beam before and after machining, where 86 layers of 1 mm thickness were removed. Speckles were applied onto the beam surface as well as onto the workpiece holder.

The raw part was positioned on the machine table with a plane connection on its bottom surface extremities. It was raised at its ends by two wedges, enabling the beam to freely deform upwards or downwards at its center. However, the positioning of the workpiece was checked with the touch probe of the machine tool in order to ensure co-linearity between the workpiece frame and the machine tool frame. The beam was also fixed onto the machine table by two flanges inserted into two slots at both beam ends. Clamping was controlled via a torque wrench set to at 60 N.m, leading to a 10 kN effort on each sloth. The workpiece mounting setup is depicted in Fig.(9).

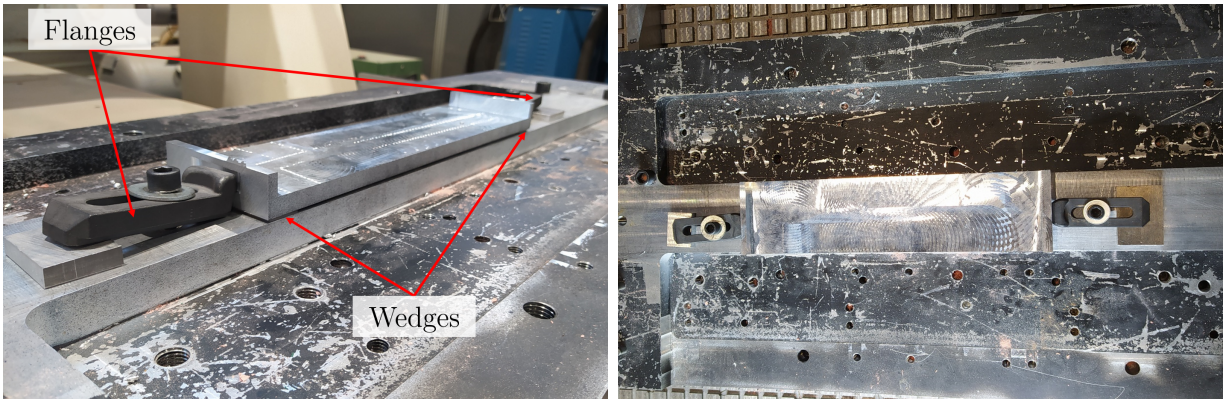

(a) Front view of the mounting setup.

(b) Top view of the mounting setup.

Figure 9: Workpiece mounting setup. The pictures were taken at the end of the machining procedure.

87 pictures were taken with a 5-DSR Canon camera equipped with a TAMRON 90 mm F2.8 Di MACRO 1:1 VC USD lens. The camera was directly mounted onto the machine table by a dedicated support. The monitored surface of the beam was enlightened with a dedicated lighting system, which was mounted onto the machine-table. The experimental setup is illustrated in Fig.(10).

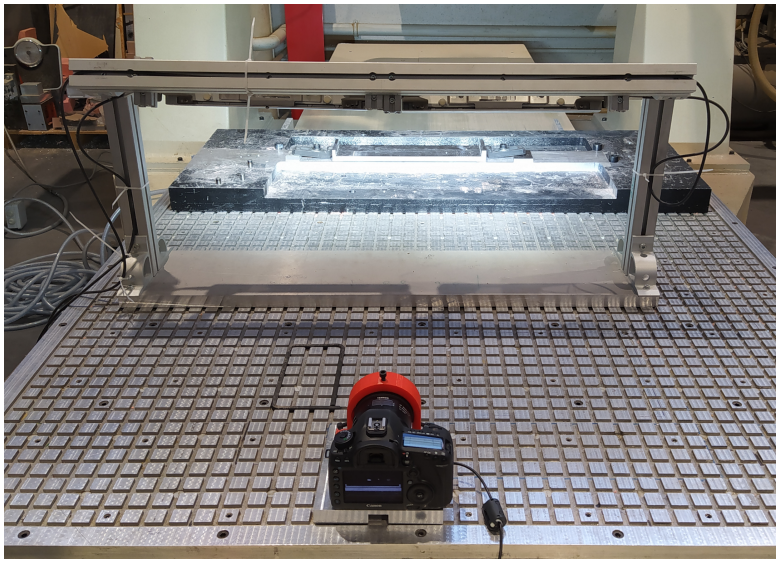

Figure 10: Experimental setup with the machine tool, the camera and the lighting system mounted on the machine-table, and the machined workpiece. The picture was taken at the end of the machining procedure.

5 Results

The displacement fields along the $\overline{x}$- and $\overline{y}$-axis, solely due to the residual stress release were obtained for the 86 deformed pictures. As a typical example, Fig.(11) and (12) illustrate the displacement fields $\overline{u_{Part_x}}$ and $\overline{u_{Part_y}}$ retrieved from the pair of pictures $1-68$.

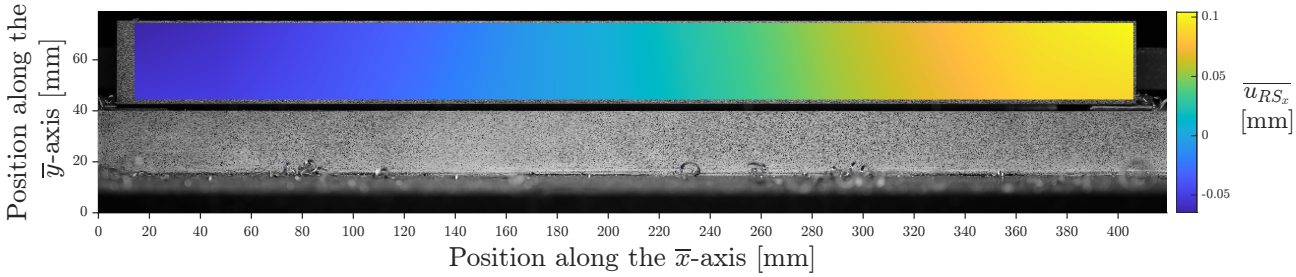

Figure 11: Displacement field $\overline{u_{RS}}$ measured along the $\overline{x}$-axis due to the residual stress release, after the machining of the 68^{th} layer.

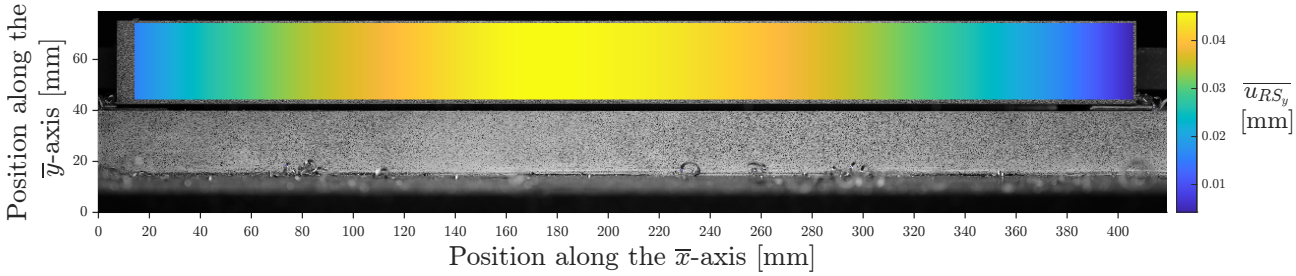

Figure 12: Displacement field $\overline{u_{RS}}$ measured along the $\overline{y}$-axis due to the residual stress release, after the machining of the 68^{th} layer.

The optical residual $\mathbf{\Psi}$ is usually checked in order to validate the obtained results, since it represents the value minimized by the GDIC algorithm. Fig.(13) represents the optical residual at convergence for the pair of pictures $1 - 68$.

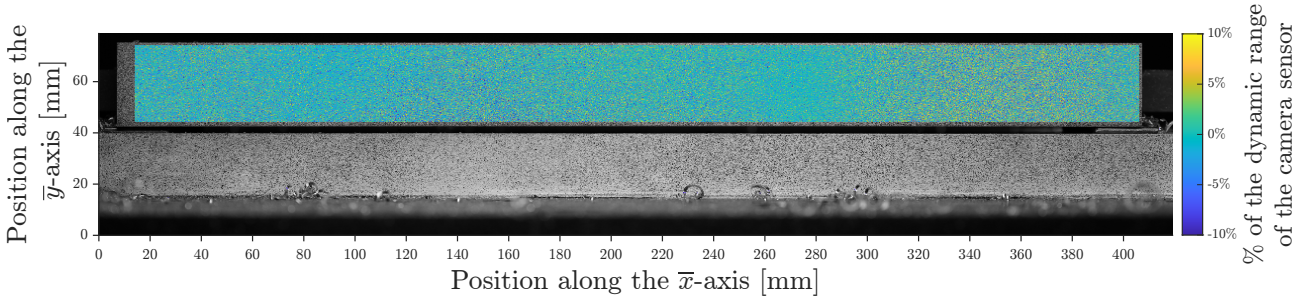

Figure 13: Optical residual $\mathbf{\Psi}$ after the machining of the 68^{th} layer. It is plotted between $\pm 10\%$ of the dynamic range of the camera sensor.

The residual map presented in Fig.(13) can be considered as homogeneous enough to conclude that convergence has been reached. However, some zones are noisier. Despite the implementation of a filter [8], metal chips are present in the pictures and disturb the optical flow. Moreover, the brightness is uneven along the beam, particularly near the beam ends.

Fig.(14) represents the evolution of the location of the neutral axis of the beam during the machining process.

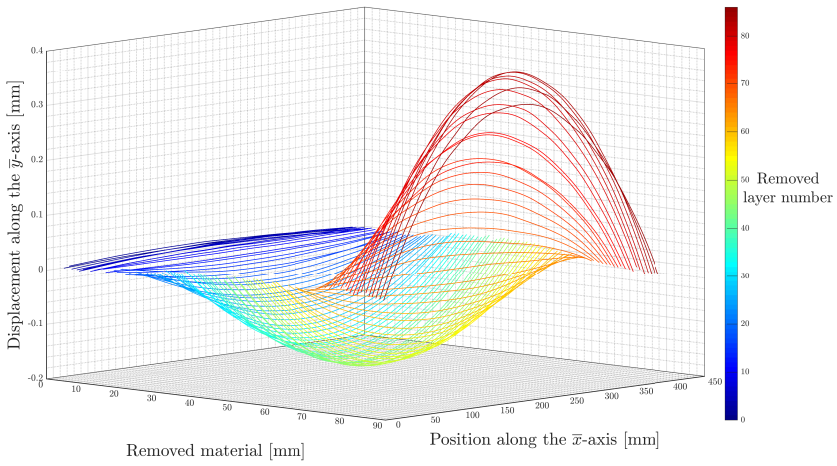

Figure 14: Evolution of the deflection of the neutral axis of the beam throughout the milling step. The beam firstly deforms slightly upwards, then backwards (reaching a minimum value), again upwards (reaching a maximum value) and finally backwards.

A first remark is that the embedding connections at the beam ends are not rigid as they are rotating around the $\overline{z}$-axis. Hence, each deflection of the neutral axis of the beam corresponds to a second order polynomial $\overline{u_{RS}}(\overline{x_P}).\overline{y} = a_1x^2+a_2x+a_3$. The middle beam curvature is identified for each polynomial expression. The curvature at the middle is equal to $\gamma_{Middle} = \dfrac{\partial^2\overline{u_{RS}}}{\partial x^2}(\overline{x_P})$, giving therefore $\gamma_{Middle} = 2a_1$. The obtained middle beam curvature after each layer removal is illustrated Fig.(15). Since the machining is performed piecewise, the through-thickness residual stress distribution is incrementally reconstructed after each machining step, namely every 1 mm. A graphical point-by-point representation of the latter is given Fig.(16).

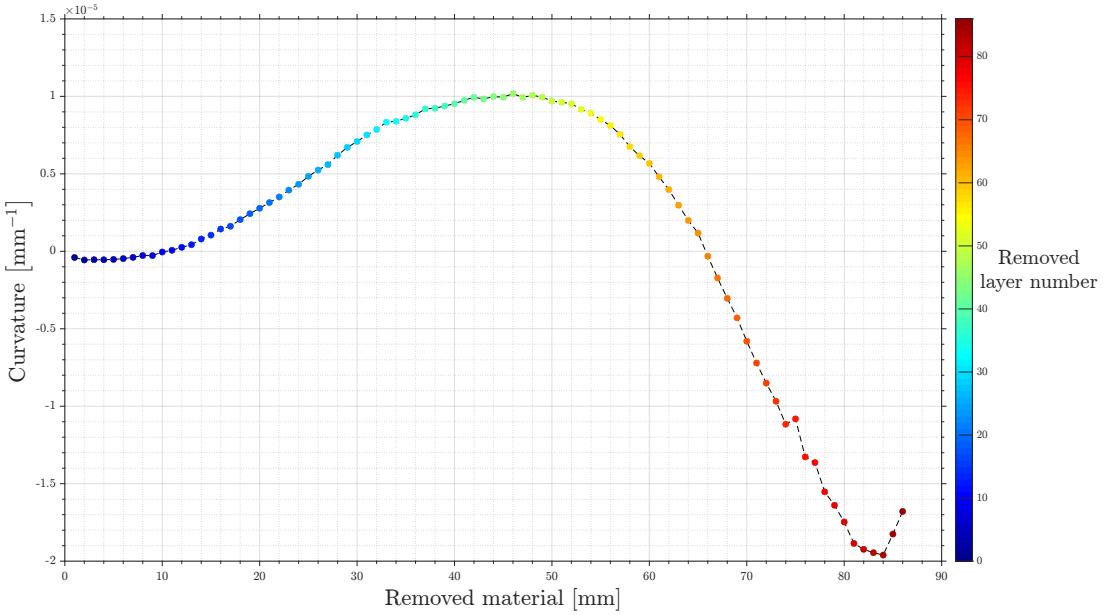

Figure 15: Evolution of the curvature at the middle of the beam throughout the machining procedure.

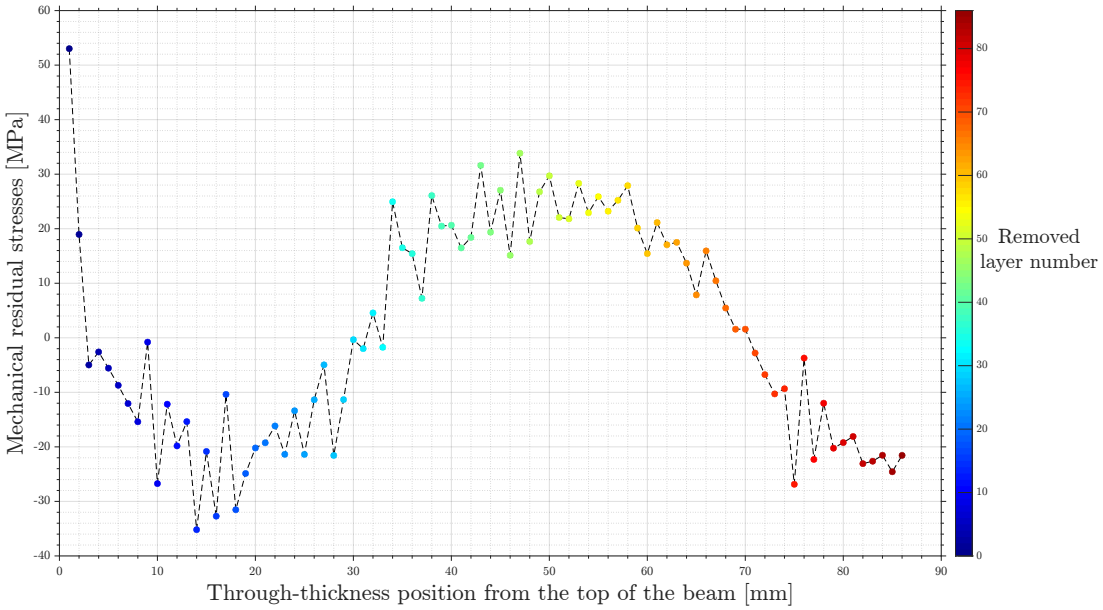

Figure 16: Initial residual stress distribution obtained while milling 86×1 mm thickness layers within a $400 \times 100 \times 100$ mm^3 Al7010-T7451 aluminum alloy beam.

6 Discussion

6.1 Comparison with results from the literature

The identified residual stress distribution has a maximum tensile stress value at the mid-plane of the workpiece thickness. It has two maximum compressive stress values underneath the upper surface and above the lower surface. According to [26], this W-shape residual stress distribution is typical of 7000 series alloys undergoing a T7451 heat treatment. This shape is due to the different cooling rate within the material after the quenching operation as well as to the inhomogeneity within the material [27]. Nevertheless, the residual stress profiles within 7000 series alloy parts, which have undergone a T7451 heat treatment, have a local minimum at the neutral plane of the beam [26]. This is not the case in the identified distribution illustrated in Fig.(16). This may result from the internal equilibrium which cannot be fully restored during residual stress release. Indeed, both embedding connections restrict the residual stress equilibrium. The latter is perhaps not sufficiently relaxed, thus leading the workpiece not to deform enough when the half of the beam is reached when milling.

Concerning the values of the magnitude of the residual stress distribution, they depend on both the different mechanical and heat treatment processes the raw part has undergone. The workpiece under study comes from an Al7010-T7451 aluminum alloy sheet metal. In the literature, the residual stress distribution of a 80 mm thickness Al7050-T7451 aluminum alloy workpiece may be found in [26]. The residual stress map presented in this latter reference is determined thanks to the so-called crack-compliance method. It may be used for comparison

purpose because both the specimens have undergone the same heat treatment processes. First, the global W-shape distribution is noticeable. Concerning the value of the magnitude, the residual stress distribution retrieved here lies between -35 MPa and 34 MPa. The distribution proposed in [26] diminishes the bounds to -18 MPa / 18 MPa. This difference is mainly due to the thicknesses of the beam, which is different from one case to another (100 mm and 80 mm respectively). Indeed, PRIME has also shown that for the same aluminum alloy undergoing the same heat treatment, higher residual stress values were observed for a thicker metal sheet. A comparison between two beams featuring a thickness respectively equal to 80 mm and 25 mm, may be found in [26].

Fig.(17) represents a comparison between the identified stress maps and its counterpart found in the literature [26]. The thickness is normalized, thus the curves lie between 0 and 1 in order to compare the amplitudes of the stresses between these two cases. It is also significant to point out that the error of measurement results is mainly influenced by the quality of the retrieved displacement field. Since the calculation of the residual stress distribution is based on the measurement of the displacement field, the error is mostly due to the measuring device. To name a few, the camera, the sensor resolution, the quality of the applied speckle, the variation of the optical flow between two pictures and the interpolation error within the computing software are known sources of errors.

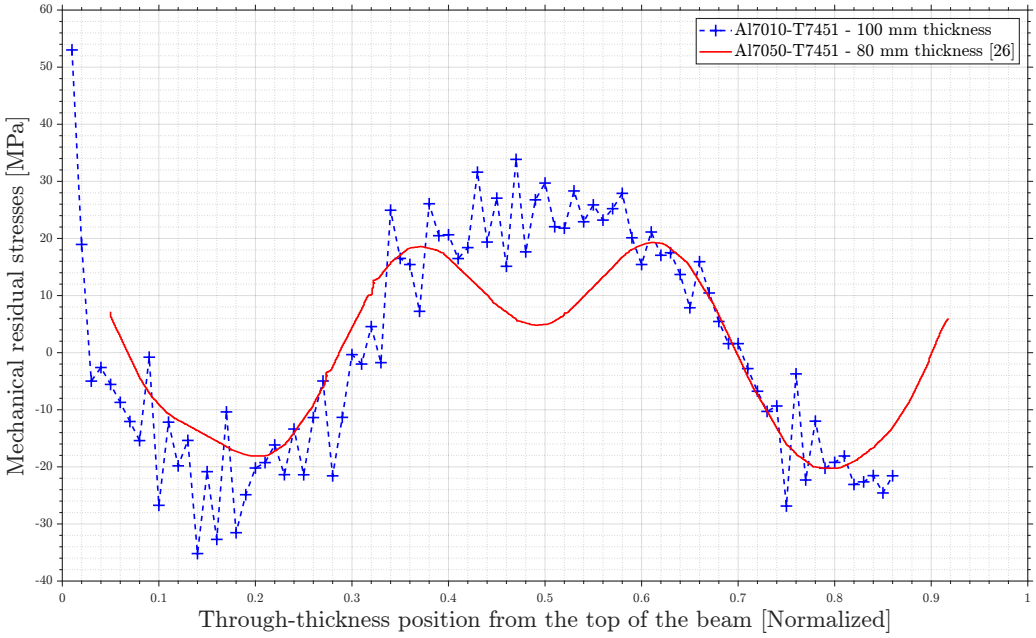

Figure 17: Comparison between initial residual stress distributions obtained with a Al7010-T7451 and a Al7050-T7451 [26] aluminum alloy beams. The thickness is respectively equal to 100 mm and 80 mm. The residual stress distributions are normalized with respect to their initial workpiece thickness so that the values of the magnitude are comparable.

Based on this comparison, the results obtained here can be considered as reasonable and consistent.

6.2 Finite Elements simulations

The proposed method was then numerically validated thanks to the Finite Element Analysis (FEA) software ANSYS™. The objective of this simulation was to implement as initial condition the residual stress distribution experimentally retrieved (see Fig.(16)) within a similar beam model and to compare the simulated deflection to the one retrieved with DIC. However, the

GDIC-retrieved stress map had first to be defined as a continuous function which must satisfy several properties :

- force equilibrium [2] : $\int_0^{t_0} \sigma_x(y)\mathrm{d}y = 0$,
- moment equilibrium [2] : $\int_0^{t_0} (y - \frac{t_0}{2}) \times \sigma_x(y)\mathrm{d}y = 0$,
- and symmetry along the beam thickness* : $\left(\frac{d\sigma_x}{dy}(y)\right)_{y=\frac{t_0}{2}} = 0.$

*this hypothesis is valid only if the workpiece has cooled down evenly after a quenching operation and if no pre-machining is performed [7].

These properties were projected on a polynomial basis defined as $\sigma_x(y) = \sum_{i=0}^{n} a_i y^i$ and a fitting operation based on the least squares method was performed. The obtained fitting curve is illustrated in Fig.(18).

Figure 18: Fitting operation performed to obtain the initial residual stress distribution.

The experiment was then reproduced in the FEA software performing a method similar to the one called "Level 0" in [14]. In the latter reference, the author shows that the global distortion of a workpiece being machined is mainly caused by both the final geometry of the part and the reorganization of the initial residual stress distribution. In this context, the complex simulation of the machining was reduced to 86 beam models of dimensions $400 \times 100 \times (100 - i_{Layer})\,\mathrm{mm}^3$ with $i_{layer} = \{1, ..., 86\}$ to reproduce the 86 machining states. SOLID185 elements of dimensions $5 \times 2 \times 1\,\mathrm{mm}^3$ were used to mesh the different models. The benefit of using these elements is that the residual stress distribution may be provided as an initial internal condition.

Concerning the boundary conditions, the movement of the workpiece ends were restricted by two pivot connections in order to reproduce the positioning system of the experiment. The aim was to let the workpiece to freely deform at its center, as described in Section (4). Concerning the loading conditions, a 10 kN force was applied onto each slot at each of the two beam ends. The objective was to model the pressure applied by the flanges on the workpiece. Then, the fitted curve of the residual stress distribution from Fig.(18) was provided as beam initial state. For each machining state, a static analysis was performed and the deflection of the neutral axis of the modeled beam was collected. Finally, the successive curvatures at the middle of the beam were determined and compared with those obtained from the experiment. This comparison is illustrated Fig.(19).

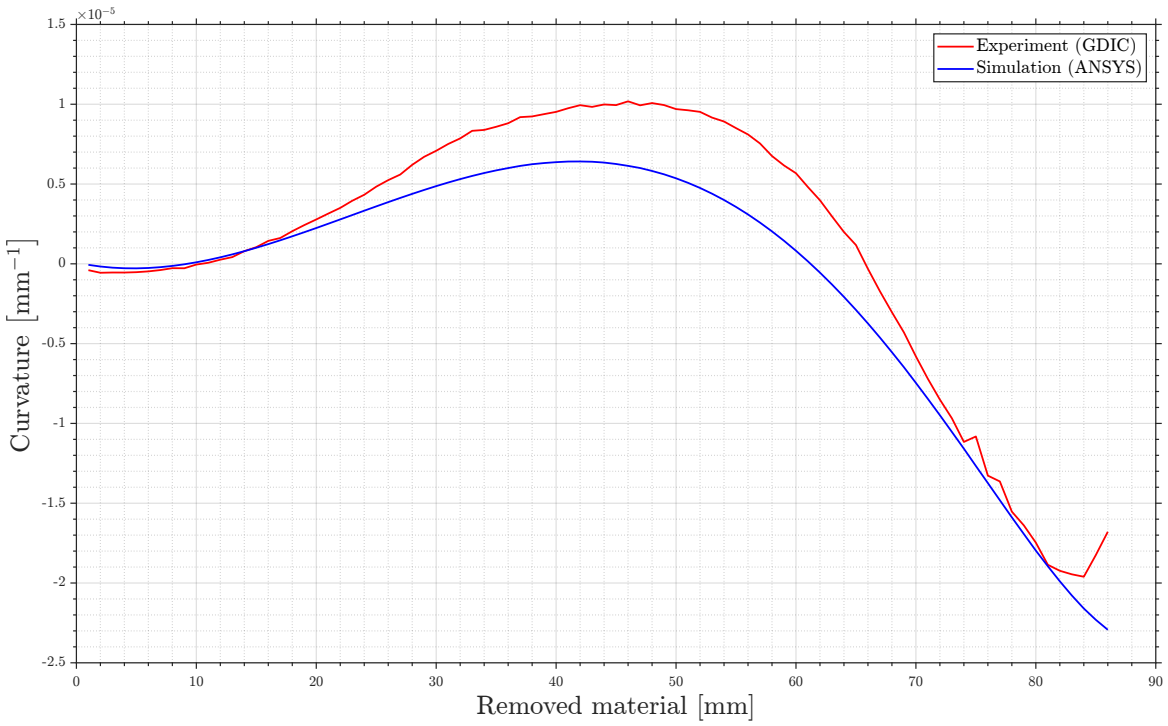

Figure 19: Comparison of the curvature at the middle of the beam obtained with GDIC and FE simulation.

The curve obtained with the simulation has the same trend as the one from the experiment. For the first twenty and the last twenty removed layers, the curve retrieved by running a FEA is close to the one obtained with DIC. However, the middle zone slightly differs from the experiment. It comes from the residual stress distribution implemented as initial beam state. Indeed, as explained in Section (6.1), the residual stress distribution in Al7XXX-T7451 aluminum alloys has a local minimum at the center plane of the beam. However, the initial residual stress distribution used in the simulation was based on the results obtained with GDIC, more specifically on a fitting curve, which does not have the typical local minimum. However, despite this difference, we can state that the precautions taken during the experiment concerning

the positioning system as well as the clamping system are consequently validated along with the proposed method.

7 Conclusion

A novel approach was developed to account for the effect of residual stresses on the geometry of a workpiece subjected to milling operations. This method merges the well-known residual stress measurement technique called Layer Removal Method, where its machining strategy is adopted as well as its mathematical formulation, and a global non-contact full-field measurement method, namely Global Digital Image Correlation. Thanks to a suitable deformation model, this method allows to retrieve the displacement fields of a machined workpiece and to identify the initial residual stress distribution along the workpiece depth with a magnitude order lying between -35 MPa and 34 MPa. The major advantage of this method is that the workpiece remains clamped throughout the procedure unlike the traditional Layer Removal Method, which obliges successive unmounting operations for curvature measurement. Letting the workpiece clamped also allows to preserve the initial workpiece positioning on the machine-table while machining. The retrieved initial residual stress distribution presents the same typical W-shape of aluminum alloy undergoing a T7451 heat treatment. The proposed method is validated by comparing the magnitude of the residual stress distribution measured here with traditional residual stress measurements from the literature. Finite Element simulations were also performed by providing the retrieved residual stress map as initial condition, in order to contrast FE displacements with those obtained during the experiment. The present study paves

the way for future more ambitious tasks, for instance measuring three-dimensional deformations during machining, retrieving bi-axial residual stress maps, and eventually adjusting in live the machining sequence to get rid of the effect of residual stresses on the final geometry of workpieces.

Acknowledgements The authors are grateful to the French National Agency (ANR) for its financial support (IMaDe project, N°ANR-19-CE10-0002-02).

Appendix A 2D-Beam element shape functions

We discuss here the displacement field of the 2D-beam elements used to discretize the workpiece. For further details, an interested reader is invited to refer to [25] from which the following equations are drawn. Let us consider a beam element of length L_k with two nodes having six DoFs each. Let us also consider that this beam-element undergoes axial, torsional and bending loading. The local reference of the beam is chosen such that the beam is defined along the $\overline{x}$-axis, as described in Fig.(7). The deformation at a material point of the cross-section, with initial coordinates (x, y, z), is defined along the $\overline{x}$-, $\overline{y}$- and $\overline{z}$-axis as $[U\ V\ W]^T$. These quantitites are defined as followed [25] :

$$\begin{cases} U(x,y,z) = u(x) - y \times \left(\dfrac{\partial v}{\partial x}\right) - z \times \left(\dfrac{\partial w}{\partial x}\right) \\ V(x,y,z) = v(x) - z \times \theta_x(x) \\ W(x,y,z) = w(x) + y \times \theta_x(x) \end{cases} \tag{A.1}$$

where (u, v, w) are the translations respectively along the $\overline{x}$-, $\overline{y}$- and $\overline{z}$-axis.

Due to bending and transverse shear, v and w both feature a bending component (respectively denoted by v_b and w_b), and a shear component (respectively denoted by v_s and w_s). Hence, the partial derivatives from Eq.(A.1) can be expressed as follows :

$$\begin{cases} \dfrac{\partial v}{\partial x} = \dfrac{\partial v_b}{\partial x} + \dfrac{\partial v_s}{\partial x} = \theta_z(x) + \gamma_{xy} \\ \\ \dfrac{\partial w}{\partial x} = \dfrac{\partial w_b}{\partial x} + \dfrac{\partial w_s}{\partial x} = -\theta_y(x) + \gamma_{xz} \end{cases} \tag{A.2}$$

The dimensions of the beam cross-section are small compared to the length of the beam. The Euler-Bernoulli hypothesis is also supposed to be satisfied. It means that cross-sections are assumed to be straight, inextensible and perpendicular to the neutral plane of the beam, before and after deformation. Consequently, Eq.(A.2) can be simplified, which gives :

$$\gamma_{xy} = 0 = \gamma_{xz} \leftrightarrow \begin{cases} \dfrac{\partial v}{\partial x} = \theta_z(x) \\ \\ \dfrac{\partial w}{\partial x} = -\theta_y(x) \end{cases} \tag{A.3}$$

Finally, the displacement field defined by Eq.(A.1) is reduced to a 2D-problem and the influence of the torsion around $\overline{x}$-axis (θ_x) is neglected. Consequently, Eq.(A.1) becomes :

$$\begin{cases} U(x, y) = u(x) - y \times \theta_z(x) \\ \\ V(x, y) = v(x) \end{cases} \tag{A.4}$$

In order to define the shape functions associated to the 2D-beam element, the functions $u(x)$, $v(x)$ and $\theta_z(x)$ must be determined with respect to the dimensions of the beam-element

and the DoFs of its nodes $\mathbf{e} = (u_i, v_i, \theta_i, u_j, v_j, \theta_j)^T$. u is taken as the form $u(x) = a_0 + a_1 x$, such that it is the solution of $ES\left(\frac{d^2u(x)}{dx^2}\right) = 0$ (with $0 \leq x \leq L_k$, E the Young's modulus and S the beam cross-section) and with boundary conditions $u(x = 0) = u_i$ and $u(x = L_k) = u_j$. The displacement is therefore defined as follows :

$$u(x) = (1 - \xi)u_i + \xi u_j \tag{A.5}$$

where $\xi = \frac{x}{L_k}$ is the normalized coordinate.

Concerning the displacement along the $\overline{y}$-axis, $v(x)$ must be C^1-continuous (in the case of an Euler-Bernoulli beam) so that the continuity of the displacement field and its first derivatives at the nodes is ensured. In order to interpolate the four remaining DoFs $(v_i, \theta_i, v_j, \theta_j)$, at least a third order polynomial is required. In fact, this amounts to find a solution of the Euler-Bernoulli homogenous equation, in the case for which the loading distribution is null [28] : $ES\left(\frac{d^4v}{dx^4}\right) = 0$. Consequently, v and its derivative θ_z can be expressed as follows :

$$\begin{cases} v(x) = b_0 + b_1 x + b_2 x^2 + b_3 x^3 \\ \theta_z(x) = \dfrac{dv(x)}{dx} = b_1 + 2b_2 x + 3b_3 x^2 \end{cases} \tag{A.6}$$

Using the following boundary conditions :

$$\begin{cases} v(x = 0) = v_i \\ v(x = L_k) = v_j \end{cases} \text{ and } \begin{cases} \theta_z(x = 0) = \theta_i \\ \theta_z(x = L_k) = \theta_j \end{cases} \tag{A.7}$$

Eq.(A.6) is solved and the following expressions are obtained :

$$\begin{cases} v(x) = Av_i + B\theta_i + Cv_j + D\theta_j \\ \\ A = 1 - 3\xi^2 + 2\xi^3 \\ \\ B = L_k\xi(1 - 2\xi + \xi^2) \\ \\ C = \xi^2(3 - 2\xi) \\ \\ D = L_k\xi^2(\xi - 1) \end{cases} \quad \text{and} \quad \begin{cases} \theta_z(x) = Ev_i + F\theta_i + Gv_j + H\theta_j \\ \\ E = \frac{6}{L_k}(\xi^2 - \xi) \\ \\ F = 1 - 4\xi + 3\xi^2 \\ \\ G = \frac{6}{L_k}(\xi - \xi^2) \\ \\ H = 3\xi^2 - 2\xi \end{cases} \tag{A.8}$$

Eq.(A.5) and (A.8) are commonly rewritten in the following matrix form $[U\ V]^T = \mathbf{N} \cdot \mathbf{e}$:

$$\begin{bmatrix} U \\ V \end{bmatrix} = \begin{bmatrix} 1 - \xi & 0 \\ 6\eta(\xi - \xi^2) & 1 - 3\xi^2 + 2\xi^3 \\ L_k\eta(-1 + 4\xi - 3\xi^2) & L_k\xi(1 - 2\xi + 3\xi^2) \\ \xi & 0 \\ 6\eta(\xi^2 - \xi) & \xi^2(3 - 2\xi) \\ L_k\eta(-3\xi^2 + 2\xi) & L_k\xi^2(\xi - 1) \end{bmatrix}^T \begin{bmatrix} u_i \\ v_i \\ \theta_i \\ u_j \\ v_j \\ \theta_j \end{bmatrix} \tag{A.9}$$

where $\xi = \dfrac{x}{L_k}$ and $\eta = \dfrac{y}{L_k}$ are the normalized coordinates.

References

[1] U. Chandra and S. Das. *Handbook of Aluminium : Physical Metallurgy and Processes*, volume 1. Springer, 2003.

[2] W. Cheng and I. Finnie. *Residual Stress Measurement and The Slitting Method*. Springer, 2007.

[3] D.M. Bowden and J.E. Halley. Aluminium Reliability Improvment Program-Final Report 60606. *Chicago, IL, USA: The Boeing Company*, 2001.

[4] P. Lequeu, P. Lassince, T. Warner, and G. M. Raynaud. Engineering for the Future: Weight Saving and Cost Reduction Initiatives. *Aircraft Engineering and Aerospace Technology*, 73(2):147–159, 2001.

[5] J. Lu, M. James, and G. Roy. *Handbook of Measurement of Residual Stresses*. Springer, Lilburn, Georgia,USA, 1996.

[6] R.G. Treuting and W.T. Read. A Mechanical Determination of Biaxial Residual Stress in Sheet Materials. *Journal of Applied Physics*, 22(2):130–134, 1951.

[7] I. Cherif, D. Cotton, G. Poulachon, J. Outeiro, A. Brosse, and J. Rebelo Kornmeier. Instrumented Clamping Device and Numerical Simulations to Study Machining Distortion. *International Journal of Advanced Manufacturing Technology*, 105(7-8):3093–3103, 2019.

[8] G. Rebergue, B. Blaysat, H. Chanal, and E. Duc. In-situ Measurement of Machining Part Deflection with Digital Image Correlation. *Measurement*, 187, 2022.

[9] W. Gao, H. Haitjema, F. Z. Fang, R. K. Leach, C. F. Cheung, E. Savio, and J. M. Linares. On-machine and In-process Surface Metrology for Precision Manufacturing. *CIRP Annals*, 68(2):843–866, 2019.

[10] P. Zhu, C. Zhang, and J. Zou. Digital Image Correlation for Sensing Kinematic Fields in Manufacturing Processes: A Review. *Journal of Intelligent Manufacturing and Special Equipment*, 2(2):37–62, 2021.

[11] A. Baldi. On the Implementation of the Integral Method for Residual Stress Measurement by Integrated Digital Image Correlation. *Experimental Mechanics*, 59:1007–1020, 2019.

[12] S.D. Salehi, M.A. Rastak, M.M. Shokrieh, L. Barrallier, and R. Kubler. Full-Field Measurement of Residual Stresses in Composite Materials Using the Incremental Slitting and Digital Image Correlation Techniques. *Experimental Mechanics*, 60(9):1239–1250, 2020.

[13] F. Hospers and L.B. Vogelesang. Determination of Residual Stresses in Aluminum-alloy Sheet Material. *Experimental Mechanics*, 15:107–110, 1975.

[14] P. Rambaud. *Computational modelling of post machining distortions of aluminium aeronautical parts : application to thin walls*. PhD thesis, Université Paris sciences et lettres, 2019.

[15] A. Öchsner. *Classical Beam Theories of Structural Mechanics*. Springer, Cham, 1 edition, 2021.

[16] M.H. Protter and Jr. C.B. Morrey. *Intermediate Calculus, Second Edition*. Springer, 1985.

[17] I. Yamaguchi. A Laser-Speckle Strain Gauge. *journal of Physics E: Scientific Instruments*, 14:1270–1273, 1981.

[18] M.A. Sutton, J.J. Orteu, and H.W. Schreier. *Image Correlation for Shape, Motion and Deformation Measurements*. Springer, 2009.

[19] B. Pan, H. Xie, and Z. Wang. Equivalence of Digital Image Correlation Criteria for Pattern Matching. *Applied Optics*, 49(28):5501–5509, 2010.

[20] B. Blaysat, J. Neggers, M. Grédiac, and F. Sur. Towards Criteria Characterizing the Metrological Performance of Full-field Measurement Techniques: Application to the Comparison Between Local and Global Versions of DIC. *Experimental Mechanics*, 60(3):393–407, 2020.

[21] J. Neggers. *Ductile Interfaces in Stretchable Electronics : Multi-Scale Mechanics and Inverse Methods*. PhD thesis, Eindhoven: University Of Technology, 2013.

[22] F. Hild and S. Roux. Comparison of Local and Global Approaches to Digital Image Correlation. *Experimental Mechanics*, 52(9):1503–1519, 2012.

[23] S.M. Looij-Kleinendorst. *Image Based Mechanical Characterization Methods For Stretchable Electronic Interconnects*. PhD thesis, Eindhoven: University Of Technology, 2019.

[24] F. Hild, S. Roux, R. Gras, N. Guerrero, M.E. Marante, and J. Flórez-López. Displacement Measurement Technique for Beam Kinematics. *Optics and Lasers in Engineering*, 47(3-4):495–503, 2009.

[25] A. Bazoune, Y. A. Khulief, and N. G. Stephen. Shape functions of three-dimensional Timoshenko beam element. *Journal of Sound and Vibration*, 259(2):473–480, 2003.

[26] M.B. Prime and M.R. Hill. Residual Stress, Stress Relief, and Inhomogeneity in Aluminum Plate. *Scripta Materialia*, 46(1):77–82, 2002.

[27] S. Dreier and B. Denkena. Determination of Residual Stresses in Plane Material by Layer Removal with Machine-integrated Measurement. *Procedia CIRP*, 24(C):103–107, 2014.

[28] I.M. Smith, D.V. Griffiths, and L.M. Margetts. *Programming The Finite Element Method - Fifth Edition.* Springer, 2014.